Supporting Information

Gate-Tunable Conducting Oxide Metasurfaces

Yao-Wei Huang[1,2,3,†], Ho Wai Howard Lee[1,2,†,+], Ruzan Sokhoyan[1], Ragip A. Pala[1,2], Krishnan Thyagarajan[1,2], Seunghoon Han[1,4], Din Ping Tsai[3,5], and Harry A. Atwater[1,2,]*

[1]Thomas J. Watson Laboratories of Applied Physics, California Institute of Technology, Pasadena, California 91125, United States

[2]Kavli Nanoscience Institute, California Institute of Technology, Pasadena, California 91125, United States

[3]Department of Physics, National Taiwan University, Taipei 10617, Taiwan

[4]Samsung Advanced Institute of Technology, Samsung Electronics, Suwon-si, Gyeonggi-do 443-803, Republic of Korea

[5]Research Center for Applied Sciences, Academia Sinica, Taipei 11529, Taiwan

* Corresponding author. E-mail: haa@caltech.edu

† These authors contributed equally to this work.

+ Current address: Department of Physics, Baylor University, Waco, Texas 76798, United States; The Institute for Quantum Science and Engineering, Texas A&M University, College Station, Texas 77843, United States

1. Optical Properties of ITO in Experiment

To characterize ITO, we perform ellipsometric and Hall measurements. These measurements confirm that the dielectric permittivity of ITO can be well described by the Drude model $\varepsilon_{ITO} = \varepsilon_\infty - \omega^2_p/(\omega^2 + i\omega\Gamma)$, where ω_p is the plasma frequency which is related to the carrier density N and electron effective mass m^* as $\omega_p^2 = Ne^2/(\varepsilon_0 m^*)$. Here ε_0 is the dielectric permittivity of vacuum, e is the electron charge, and Γ is the damping constant. Using literature values for the constants ($\Gamma = 1.8\times10^{14}$ radHz, $m^* = 0.35\ m_e$, and $\varepsilon_\infty = 3.9$),[1-4] we relate the charge distribution in ITO to the dielectric permittivity of ITO ε_{ITO}. The fact that ε_{ITO} can be related to the carrier concentration in ITO via the Drude model explains the key physical mechanism behind metasurface phase and amplitude modulation.

The ITO films in our experiments are deposited by RF magnetron sputtering, where the carrier concentration of ITO is varied by controlling the ratio of the Ar and O_2 flow rates during deposition.[1,5] We have two valves of gas to the chamber of sputter. One is Ar flow valve that we keep with a flow of 20 sccm. The other is the Ar+O_2 valve with the ratio of Ar and O_2 is 3:1. The optical properties of the ITO are derived from Hall and ellipsometry measurements.[6] We fabricate ITO films with background carrier concentrations ranging from $N_o = 8\times10^{19}$ cm^{-3} to 7×10^{20} cm^{-3}. To obtain ITO with pre-designed carrier concentrations (these carrier concentrations should yield Re(ε^{ITO}) = 1.5-2.5 at the wavelength of interest), we vary by a small range, the Ar+O_2 flow from 0.4 sccm to 1.6 sccm while depositing 23 nm ITO film on several different quartz substrates (for Hall measurement) and silicon substrates (for ellipsometry measurement). The carrier concentration N and electron mobility μ (thus the resistivity ρ) of the ITO films are measured using the Hall method. The complex dielectric permittivity of the ITO films in the near infrared region was measured by ellipsometry, and the raw data for the complex permittivity was fitted by a single Drude function, using the carrier concentration and mobility obtained from Hall measurements. The high frequency permittivity (ε_∞) and damping rate (τ^{-1}) are determined via fitting the Drude model to the measured data. Although, for ITO in the ultraviolet to visible region, the contribution of Lorentzian oscillators cannot be ignored in fitting the ellipsometry data, the effect of these oscillators is smaller in the near infrared and can be absorbed in the constant ε_∞. The real and imaginary part of the dielectric permittivity for different samples

deposited with different Ar+O_2 flows are shown in Fig. S1. As can be seen in Fig. S1, for the assumed experimental conditions, the real part of the dielectric permittivity of ITO is between 1.5 and 3 at the target wavelength of 1550 nm. This indicates that for experimentally achieved ITO doping levels, one can ensure via gating that the epsilon-near-zero (ENZ) condition occurs in the ITO accumulation layer. In addition, the simulated permittivity (black dashed curve) obtained from a standard Drude model with commonly used constants indicates agreement both with the slope of the dispersion and the value of the permittivity for the ITO deposited with a 1.2 sccm Ar+O_2 flow. Using these fitting parameters and the following relations:

$$\rho = \frac{1}{q\mu N} = \frac{m^* m_e}{Nq^2\tau},$$

$$\varepsilon_{ITO}(\omega) = \varepsilon_\infty - \frac{\omega_p^2}{\omega^2 + i\omega\Gamma}, \quad \omega_p^2 = \frac{Nq^2}{\varepsilon_0 m^* m_e}, \quad \Gamma = 1/\tau,$$

we find that the electron effective mass (m^*) takes values ranging from 0.3 m_e to 0.23 m_e, depending on fabrication conditions which is consistent with previously reported results.[7] The optical constants obtained from Hall and ellipsometry measurements are listed in Table S1.

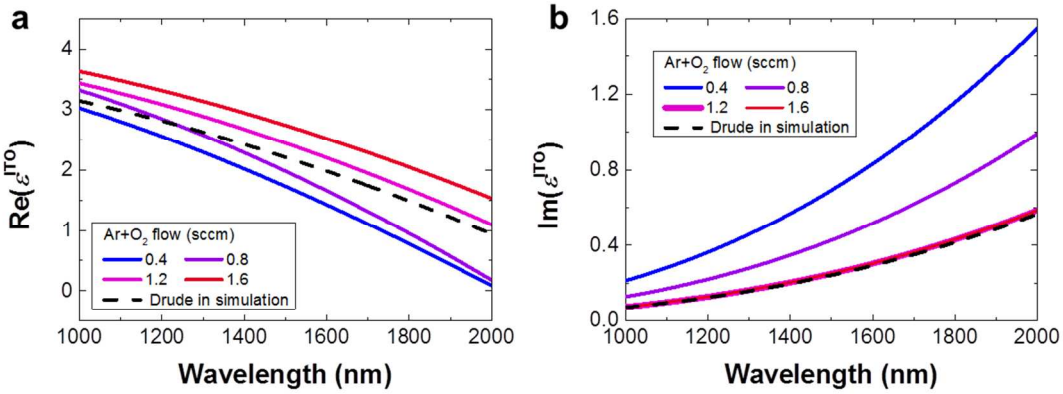

Figure S1. Solid lines represent measured real and imaginary parts of dielectric permittivity of ITO for different Ar+O_2 flow during the deposition. The dashed line corresponds to the dielectric permittivity of ITO obtained by using literature values for Drude parameters.[1-3] The constants used in the figure are listed in the Table S1.

Table S1. Electrical measurement results as well as optical Drude parameters for ITO films deposited with different $Ar+O_2$ flows. The data is obtained from the Hall and ellipsometry measurements. The literature values of ITO constants are also included in the table.[1-3]

$Ar+O_2$ flow (sccm)	0.4	0.8	1.2	1.6	Literature values
Resistivity, ρ (Ωcm)	9.8496×10^{-4}	6.2581×10^{-4}	6.8987×10^{-4}	8.4197×10^{-4}	
Mobility, μ (cm^2/Vs)	16.429	29.378	39.482	39.403	
Carrier density, N (cm^{-3})	3.8575×10^{20}	3.3953×10^{20}	2.2918×10^{20}	1.8815×10^{20}	3×10^{20}
Scattering time, τ (fs)	2.7803	4.5451	5.6858	5.1251	
Damping constant, Γ (Hz)	3.5967×10^{14}	2.2002×10^{14}	1.7588×10^{14}	1.9512×10^{14}	1.8×10^{14}
High frequency permittivity, ε_∞	4.1412	4.4195	4.2345	4.3536	3.9
Effective mass, m^*	0.2972	0.2717	0.2525	0.2284	0.35

The ITO of our device was fabricated at $Ar+O_2$ flow rate of 1.2 sccm. As one can see from Table S1, the carrier concentration of ITO in this case is $N_0 = 2.3\times10^{20}$ cm^{-3}. It has been previously observed that the carrier concentration of ITO increases during ALD process due to leakage of oxygen from ITO.[8] Since Hall measurements have been taken before ALD process, we expect the carrier concentration of ITO in our final device to be higher than the measured Hall value. To identify the ITO carrier concentration in our final device, we have performed extensive numerical simulations. Our numerical simulations show that the carrier concentration of $N_0 = 2.8\times10^{20}$ cm^{-3} provides an excellent agreement between the measured and calculated positions of the reflectance dip. Hence, in what follows we assume that the carrier concentration of ITO is $N_0 = 2.8\times10^{20}$ cm^{-3}. On the other hand, the electron affinity of ITO determines the voltage that provides 180° phase shift of the reflected light. Figure S2 shows the phase shift as a function of applied bias for different electron affinities of ITO (χ_{ITO}). When increasing the electron affinity and, consequently, the work function of ITO, the carrier concentration of ITO at the Al_2O_3/ITO interface increases. This results in reduction of voltage necessary to achieve 180° phase shift. We use electron affinity of ITO as a fitting parameter to match the bias that provides 180° phase shift of the reflected light to the experimentally observed value of 2.5 V. Our simulations show a perfect match with experimentally measured values of the phase shift (Figure 3c, blue line with green spheres) when the electron affinity of ITO is taken as $\chi_{ITO} = 5$ eV.

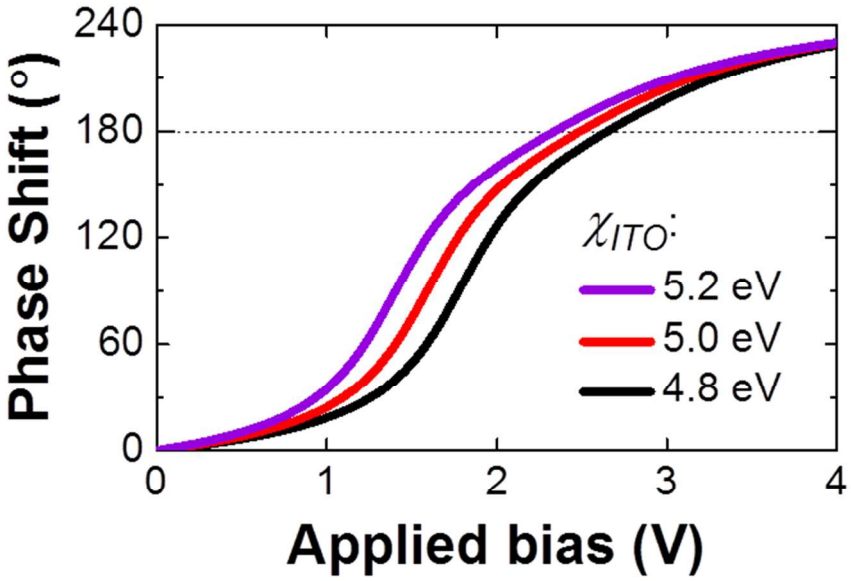

Figure S2. Simulated phase shift as a function of applied bias for different assumed electron affinities of ITO (χ_{ITO}). The operation wavelength is 1573 nm.

2. Optical Properties of ITO in Simulation

We performed electrostatic calculations to determine the electron distribution in ITO as a function of applied bias. We model ITO as a semiconductor with the bandgap of E_{bg} = 2.8 eV,[9] electron affinity of χ = 5 eV, effective electron mass of m^* = 0.25 m_e. In our calculations DC permittivity of ITO is chosen as 9.3.[10] Depending on fabrication conditions, electron mobility of ITO ranges from 16 cm^2/Vs to 38 cm^2/Vs as confirmed by Hall measurements. We assume that the electron distribution in the ITO, in case of the metasurface geometry, can be approximated by that in the case of a simple planar MOS structure consisting of infinite Au/Al_2O_3/ITO layers (Fig. 2b in the main text). For numerical modeling we used a commercial software (Device - Lumerical Solutions, Inc.) that numerically solves the Poisson and drift-diffusion equations. In the software we define Al_2O_3 as an insulator that implies that no charge flows through it. This is a valid assumption since our leakage currents are small. First, we calculate capacitance of the Au/Al_2O_3/ITO/Au planar structure assuming that the thickness of the dielectric spacer d is 5 nm, and DC permittivity of Al_2O_3 is ε_{dc} = 9. In the device physics calculations, we used the mesh size

of 0.05 nm which has been validated by performing careful convergence tests. Figure S3a shows capacitance of the $Au/Al_2O_3/ITO/Au$ device as a function of applied voltage for different background carrier concentrations of ITO. As one can see, the capacitance of the MOS capacitor increases when increasing background carrier concentration of ITO. The dependence of the capacitance on applied bias becomes weaker when ITO is more doped. If we further increase carrier concentration of the semiconductor in the MOS structure, the screening length will decrease and the capacitance of the device will asymptotically approach the capacitance of an ideal parallel plate capacitor. The plates of the ideal parallel plate capacitor are made of perfect electric conductor that ensures that electric field does not penetrate into them. Capacitance of the ideal parallel plate capacitor is given by the following well-known formula:

$$C_{\text{ideal}} = \frac{A\varepsilon_{\text{dc}}}{\varepsilon_0 d},$$

where A is the area of the capacitor plate, ε_{dc} is the dc permittivity of the dielectric spacer, ε_0 is the vacuum permittivity and d is the thickness of the dielectric spacer (see Fig. S3b). If thickness of the Al_2O_3 spacer is 5 nm then for the plate area A = 1 μm^2, C_{ideal} = 15.93 fF/μm^2. Evidently, for a given capacitor plane area, the capacitance of the MOS capacitor is lower than the capacitance of the ideal parallel plate capacitor. Indeed, using Gauss's law one can readily show that the charge accumulated at the capacitor plates is proportional to the voltage drop across the dielectric spacer. Since in case of the MOS capacitor there is also additional voltage drop inside of the semiconductor, then for any value of the applied voltage V, there will be more charge accumulated at the plates of the ideal parallel plate capacitor as compared to the case of the MOS capacitor (see inset of Fig. S3b).

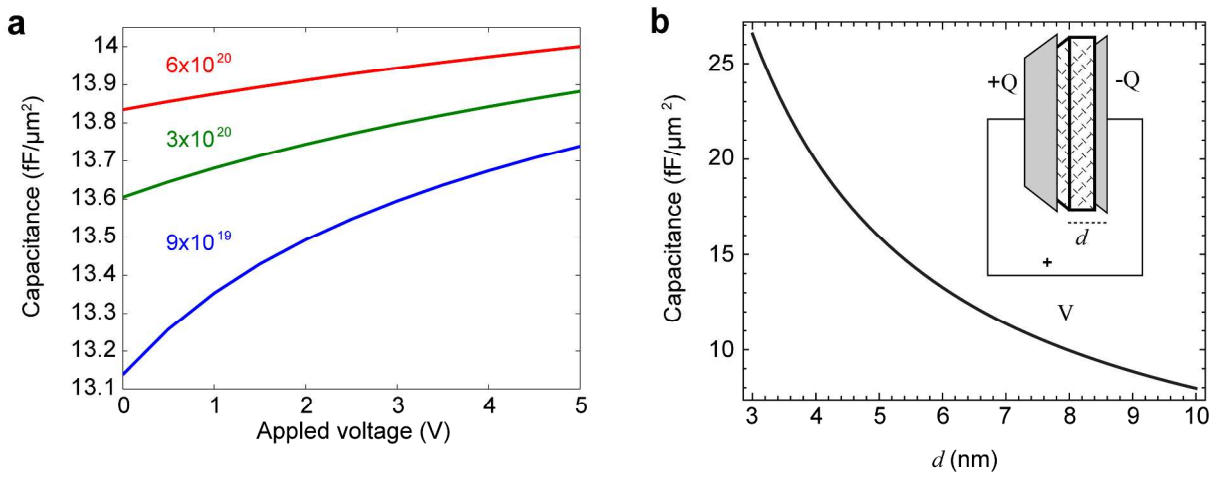

Figure S3. (a) Capacitance of the MOS capacitor as a function of applied bias for different background doping of ITO. (b) Capacitance of the ideal parallel plate capacitor as a function of the thickness of Al_2O_3 spacer. In both cases (a)-(b) gate dielectric is 5 nm thick Al_2O_3. Inset of (b) shows schematics of the parallel plate capacitor.

Figure S4 depicts carrier concentration N_0, in ITO in log-scale as a function of distance from the Al_2O_3/ITO interface at an applied bias of 2.5 V for experimentally accessible values of the background carrier concentration. As it is in the case of fabricated structures, the thickness of Al_2O_3 is 5 nm. As one can see, the spatial volume over which noticeable charge density redistribution occurs increases with decreasing background carrier concentration. Based on the calculated values of the carrier concentration as a function of applied voltage and distance from Al_2O_3/ITO interface, we calculate the dielectric permittivity of ITO ε via Drude model. Figures S5a-S5b plot real and imaginary parts of the dielectric permittivity ε as a function of the distance from Al_2O_3/ITO interface at the wavelengths of 1550 nm and for applied bias voltages of 2.5 V and 3.5 V. Each curve in Fig. S5 corresponds to the marked background carrier concentration of ITO. Apparently, for a given background carrier concentration, one observes larger variation of ε at longer wavelengths. This is due to the fact that the second term of the Drude model is proportional to $1/(\omega^2 + i\,\omega\Gamma)$.

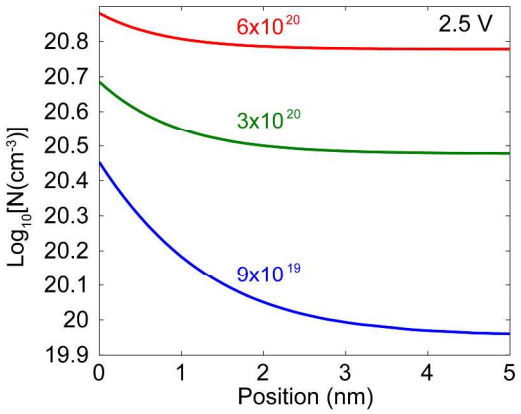

Figure S4. Log_{10} of the carrier concentration in ITO for different background doping levels (N_0 = 9×10^{19}, 3×10^{20}, and 6×10^{20}) as a function of distance from the Al_2O_3/ITO interface.

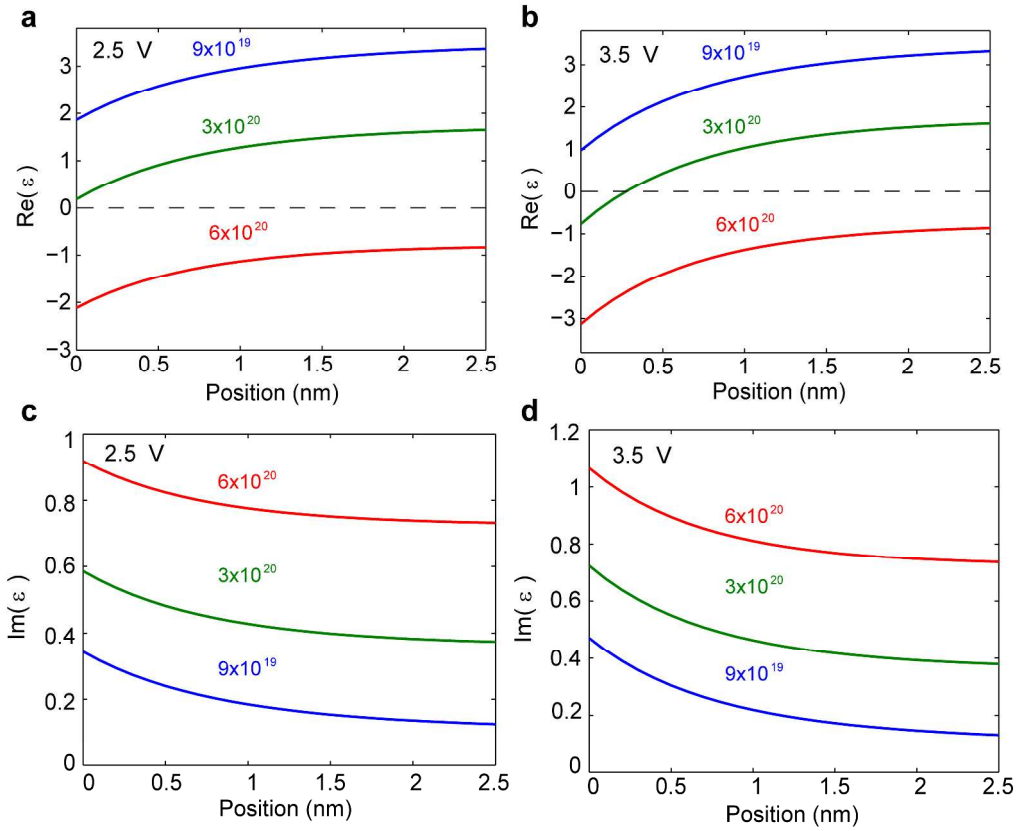

Figure S5. Calculated dielectric permittivity of ITO as a function of distance from the Al_2O_3/ITO interface at 1550 nm. (a)-(b) Real part of the dielectric permittivity of ITO at applied bias of (a) 2.5 V and (b) 3.5 V. (c)-(d) Imaginary part of the dielectric permittivity of ITO at applied bias of (c) 2.5 V and (d) 3.5 V.

Our calculations show that for the ITO background carrier concentration of $N_0 = 3\times10^{20}\text{cm}^{-3}$, the real part of the dielectric permittivity in the ITO accumulation layer changes its sign, going from positive to negative, when a large enough bias is applied. It is also shown that the carrier concentration of the ITO at the Al_2O_3/ITO interface increases by five times with applied bias from 0 to 6 V (see Fig. 1b).

Based on this knowledge, we have developed general design principles of gate-tunable conducting oxide metasurfaces. When designing a metasurface that would ensure large phase modulation of the incoming light we take the following steps: a) we choose the operation wavelength; b) we identify the background carrier concentration that will ensure ENZ transition in the accumulation layer in ITO when applying voltage; c) finalize the design of the metasurface by identifying ITO thickness and dimension of the top electrode and antenna that would ensure magnetic dipole resonance at the chosen wavelength.

3. Fabrication of tunable metasurfaces

The metasurfaces were fabricated via standard e-beam lithography and multiple thin-film depositions. Schematic of the tunable metasurface is depicted in Fig. S6a where voltage is applied between the antenna via the external gold pads and the gold back plane. The inset of Fig. S6a shows a close-up look of the stripe antenna that were designed and fabricated. Fig. S6b shows the fabrication process of our gate-tunable metasurface. A 5-nm-thick Ti film was deposited, as an adhesion layer, by thermal evaporation on a quartz glass substrate, followed by thermal evaporation of 80 nm of Au. Then 18 nm of ITO was sputtered on the sample by using RF magnetron sputtering in an oxygen/argon plasma (ITO targets were purchased from Plasmaterials Inc.). All depositions were done at room temperature at a pressure of 3 mTorr at a power of 48W, while the oxygen/argon flow rates were varied to achieve different carrier concentrations of the ITO (see ITO characterization in Supporting Information part1). A 5 nm thick Al_2O_3 was then grown by atomic layer deposition (Fiji F200, Ultratech/Cambridge NanoTech).

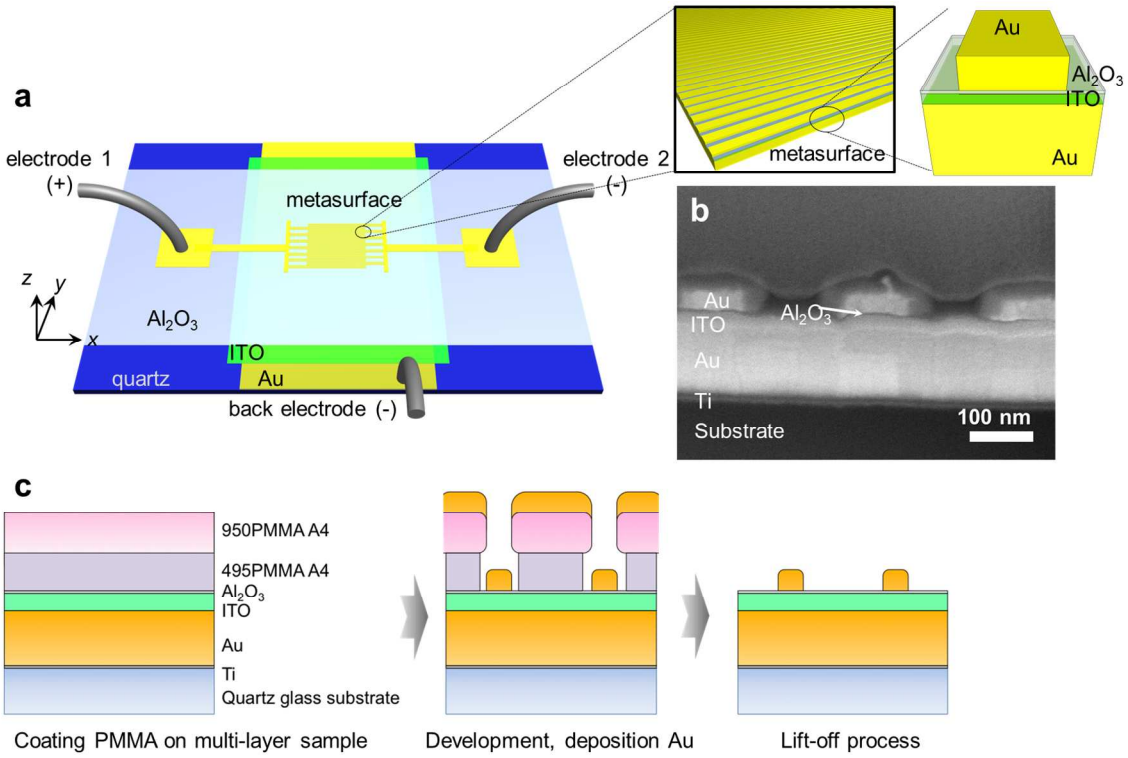

Figure S6. (a) Schematic of the tunable metasurface where voltage is applied between the stripe antenna via the external gold pads and the bottom gold mirror. (b) The cross-section of the fabricated metasurface after the lift-off process. (c) Fabrication process of the gate-tunable metasurface.

Figure S6c shows a schematic of the e-beam lithography process. After the previous steps, the sample was further coated with 300 nm of bilayer PMMA (MicroChem Corp., PMMA-495K A4 and PMMA-950K A4). Subsequently, the stripe structures with 40 × 40 μm^2 area, gold connections, and gold pads were patterned using an e-beam lithography system (Leica Vistec EBPG 5000+) at an acceleration voltage of 100 keV with 100 pA current (for antenna structure) and 50 nA current (for connections and pads). After exposure and development, a 50 nm Au film was deposited by e-beam evaporation. A combination of bottom and top layer resists is selected in such a way that there is a large difference in the dissolution rates of the layers at the development step, leading to a reversed trapezoid resist profile. The samples were eventually soaked in acetone in which the un-patterned regions were lifted off. The SEM image of the cross-section of the metasurface sample is depicted in Fig. S6b. Note that the gold antennas were

designed to connect to two isolated left and right pads so that two different voltages can be applied on the pads for demonstrating a one-dimensional 2-level phase grating with periodicity of 2.4 μm (see Fig. 1).

4. Field analysis at 0 V

When performing electromagnetic calculations the assumed mesh size is 0.27 nm. This mesh choice has been validated by performing careful convergence tests. Our electromagnetic calculations show presence of large-magnitude x component of the magnetic field $|H_x|$ localized in the gap region between gold antenna and gold back plane (see Fig. S7c) that indicates that the considered resonance is a magnetic plasmon resonance. Figure S7a (which is the same as Fig. 2d of the manuscript) shows that the z component of the electric field E_z around right edge of the antenna (blue, at y = 125 nm, z = -10 nm) is antiparallel to E_z around left edge of the antenna (red, at y = -125 nm, z = -10 nm). On the other hand, Fig. S7b shows that at the bottom of the antenna the y component of the electric field E_y is oriented in –y direction (light blue) whereas at the top of the back plane E_y is oriented +y-direction (light red). The considered resonance supports an antiparallel or curl electric field, resulting in a curl current density shown in red cones (Fig. S7b). This curl of the electric field and current density is consistent with large x component of magnetic field $|H_x|$ shown in Fig. S7c.

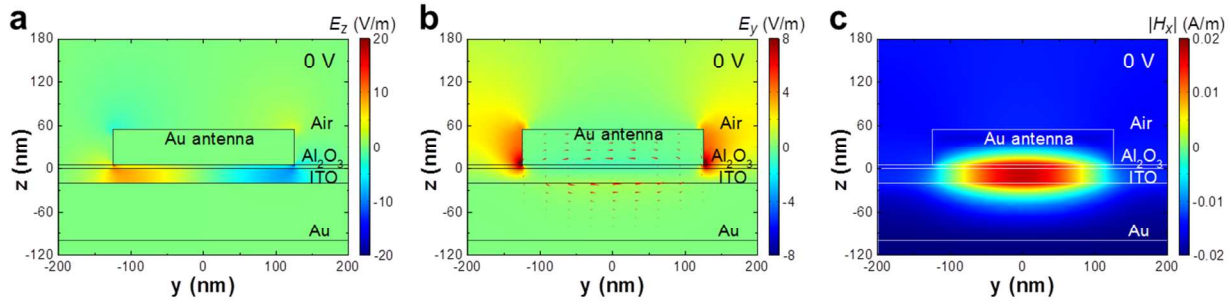

Figure S7. Spatial distribution of the z component of the electric field E_z (a), y-component of the electric field E_y with current density shown in red cone (b) and absolute value of the x component of the magnetic field $|H_x|$ (c) for applied bias of 0V.

5. Reflectance measurements

The experimental setup used to measure the metasurface reflectance spectrum is illustrated in Fig. S8. An un-collimated light from halogen lamp is collimated by using lens and directed through a polarizer and 50/50 non-polarizing beam splitter. The incident light is then focused onto the metasurface sample by using a 40×, 0.75 NA microscope objective (see inset).

The light reflected from the metasurface is diverted by a beam-splitter and sent to near-IR camera or an optical spectrometer through a multi-mode fiber. Note that the position of the metasurface is pre-adjusted by imaging with the camera so that only the light reflected from the center of the metasurface (~ 20×20 μm^2) is collected by the spectrometer. The measured reflectance is normalized relative to reflectance in the area without metasurface structure (reflected directly from the gold back plane reflector just next to the metasurface).

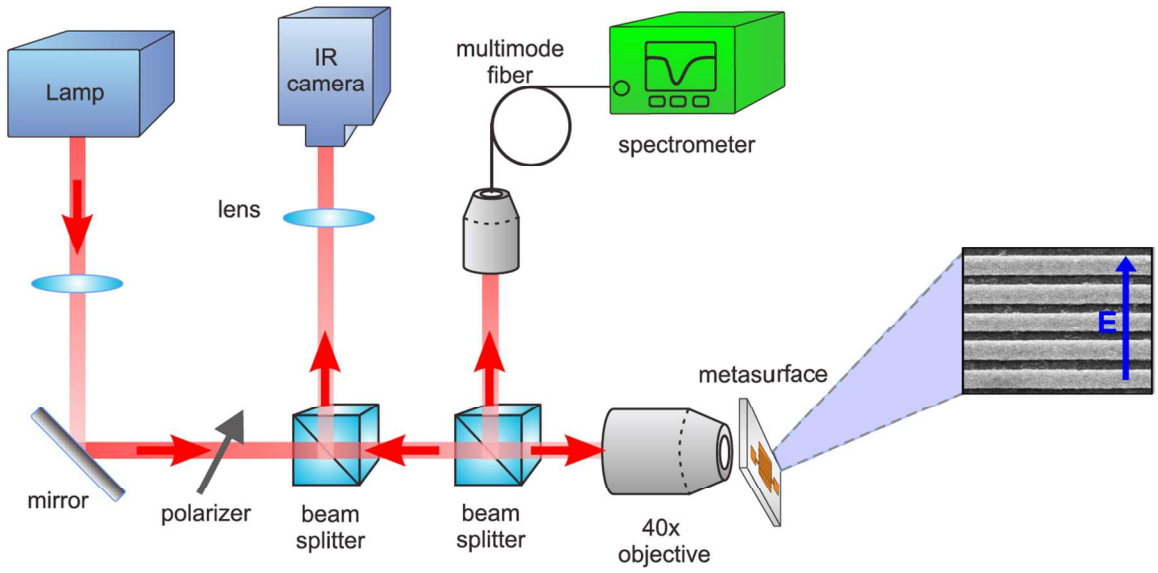

Figure S8. Optical setup for measuring the reflectance spectra of the metasurfaces. The polarization of the incident light is aligned to the *y*-axis of the sample, providing polarization-sensitive measurements.

6. Phase measurements on metasurfaces

The optical phase of light reflected from the metasurface is measured by a Michelson interferometer (Fig. S9a). A narrow-band coherent near-infrared light source (emitted by a tunable laser) is directed onto a beam splitter. One beam is focused onto the mirror mounted on a piezo-stage, while the other beam is aligned to the edge of the metasurface so that half of the beam is reflected from the metasurface and the other half from the multi-layer of Al_2O_3/ITO/Au-back-plane (reference) (Fig. S9b). The beam reflected from the sample (metasurface and reference) separately interferes with the beam in the other path that has been reflected from the mirror, resulting in the two regions of interference fringe recorded by the near-infrared camera. The optical path length between two paths can be precisely adjusted with the piezo-stage until the interference fringes are seen in the camera.

Another method to measure the phase modulation with applied bias is to capture the interference fringes for both the metasurface and reference at different positions of the Michelson mirror, using the piezo stage. Such a measurement method has been demonstrated in the past.[11] However since the piezo stage can only provide limited position accuracy, several measurements would need to be acquired (more than 100 times) to measure an accurate phase shift. We believe our method provides an easy and direct way to measure the phase modulation from the metasurfaces.

To obtain the phase shift induced by applied bias (Fig. 3c), the shift of the interference fringes under bias is measured. Figure S10a shows the interference fringes recorded by the near-infrared camera at applied bias voltages from 0 V to 2.5 V. An offset of fringes between the light reflected from the metasurface and reference is clearly seen in the case of 0V, but disappears in the case of 2.5V. To analyze the fringes, we select two cross-sections shown in Fig S10a for each image (Fig. S10b, black lines) and translate them to the smooth curves by using a moving average filter (Fig. S10b, magenta lines for metasurface and green lines for reference). Furthermore, we fit a function (sinusoidal function times a Gaussian) to each smooth curve. We use the obtained sinusoidal function to retrieve the phase at each applied bias. The fitted sinusoidal pre-factors for each smooth curve are shown in Figure S10c, where red and olive lines represent the sinusoidal pre-factors originating from the metasurface and reference, respectively.

The phase is defined as the ratio of the distance between the wave crests of metasurface and reference ($\Delta\Lambda$) and the period of the wave (Λ). The phase shift calculated in such a way will be given in units of radian. The nonzero phase shift implies that the phase under applied bias is different from the phase with no applied bias (0 V). Table S2 summarizes the values of phases and phase shifts retrieved for each applied bias. The retrieved phase shift as a function of applied bias is shown in Fig. 3c. It should be mentioned the slight variation of fitted Λ value between the two cross-sections for each interference fringes result in the phase measurement errors. The region of upper and lower error bars of phase shift (Table S2 and Fig. 3c) corresponds to the standard deviation of Λ smaller than 7%. We totally recorded 4 images for each voltage and chose several different positions of cross-sections for fitting for each image. All of them are considered for the error bars.

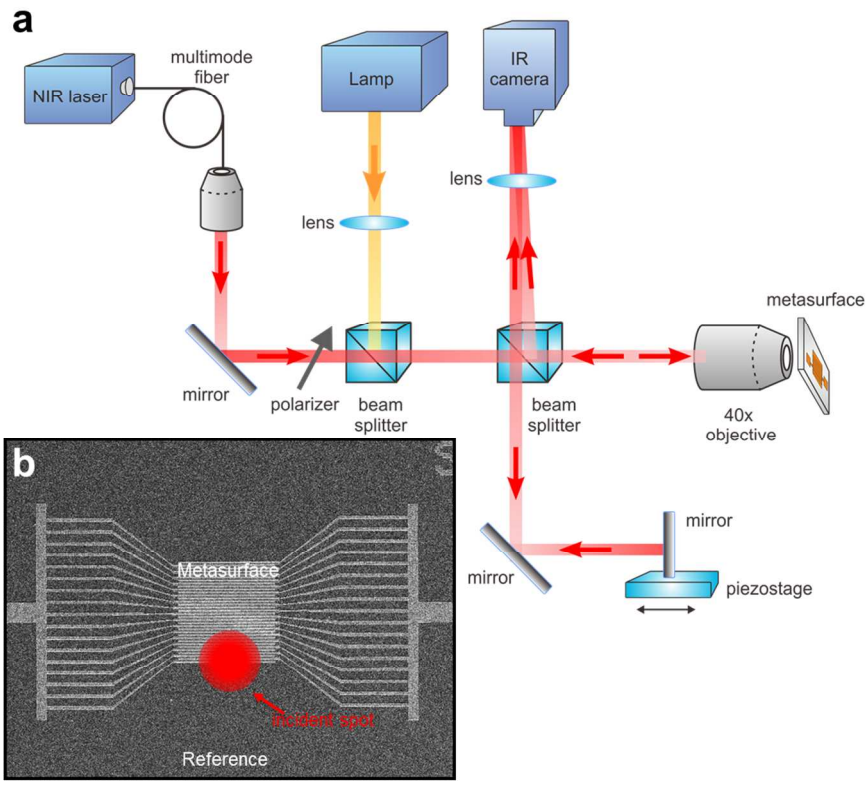

Figure S9. (a) Schematic of the optical phase measurement setup. (b) Schematic showing the position of the incident light where half of the beam is reflected from the metasurface and another half is reflected from the reference (the multi-layer stack of Al_2O_3/ITO/Au-back-plane).

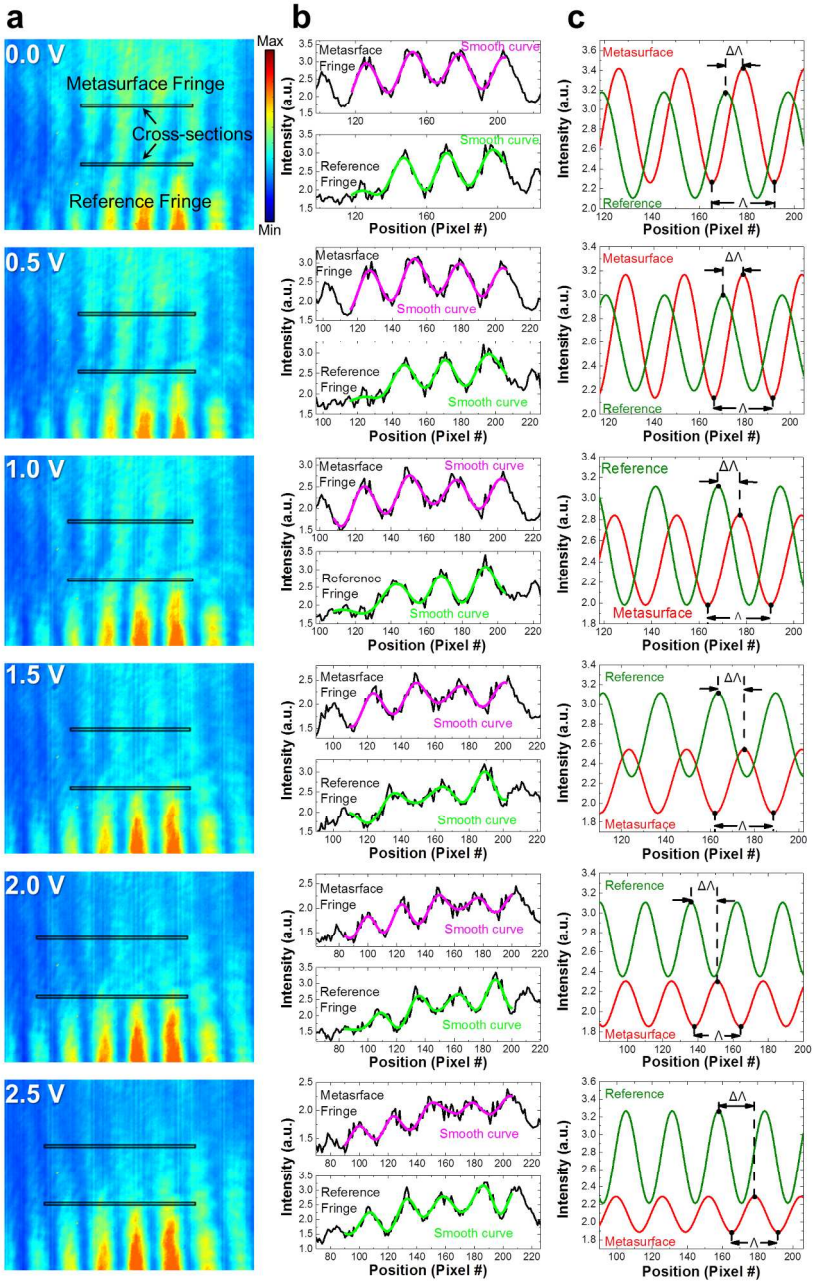

Figure S10. (a) Measured interference fringes. The upper and lower fringes originate from the metasurface and reference, respectively. (b) The raw data (black line) and smooth fitting curves (magenta line for the metasurface and green line for the reference). (c) The fitted sinusoidal waves for each smooth curve. Red line: metasurface. Olive line: reference. Λ: the period of the sinusoidal waves. ΔΛ: the distance between the peaks of the sinusoids obtained via fitting reference fringes and metasurface fringes.

Table S2. The phase and phase shift induced by applied bias from 0 to 2.5 V.

Applied Bias (V)	Phase (°)	Phase shift (°)	Error bar of phase shift (°)	
			Upper	Lower
0.0	99.0	0.0	20.5	-2.6
0.5	121.0	22.0	26.8	-43.5
1.0	121.6	22.6	30.1	-19.3
1.5	163.1	64.1	75.5	15.6
2.0	206.2	107.1	166.7	82.2
2.5	283.3	184.3	204.6	162.3

7. The structural non-uniformity and simulation

The wavelength at which phase measurements are performed (1573 nm) is shifted with respect to the resonant wavelength obtained via reflection measurements (compare Figs. 3c, 2c, and 3a). This difference is due to the fact that the reflectance measurements have been taken by illuminating the center of the sample while the phase measurements have been taken by illuminating the edge of the sample. Figure S11 shows that the resonance shifts from 1560 nm to 1585 nm depending on the part of the sample probed during the measurement (center vs. edge). During the reflectance position measurement, spot size with diameter of 5 μm is used. The taken SEM images confirm that when moving to the edge of the sample the interference fringes become wider (Fig. S11). In the simulations shown in Fig. 2a, the resonance dip is at 1557 nm yielding operation wavelength of 1550 nm. Note that the operation wavelength, that is the wavelength at which large phase shift is observed, is shifted with respect to the resonant wavelength. In the phase shift simulations shown in Fig. 3c, the operation wavelength is 1573 nm.

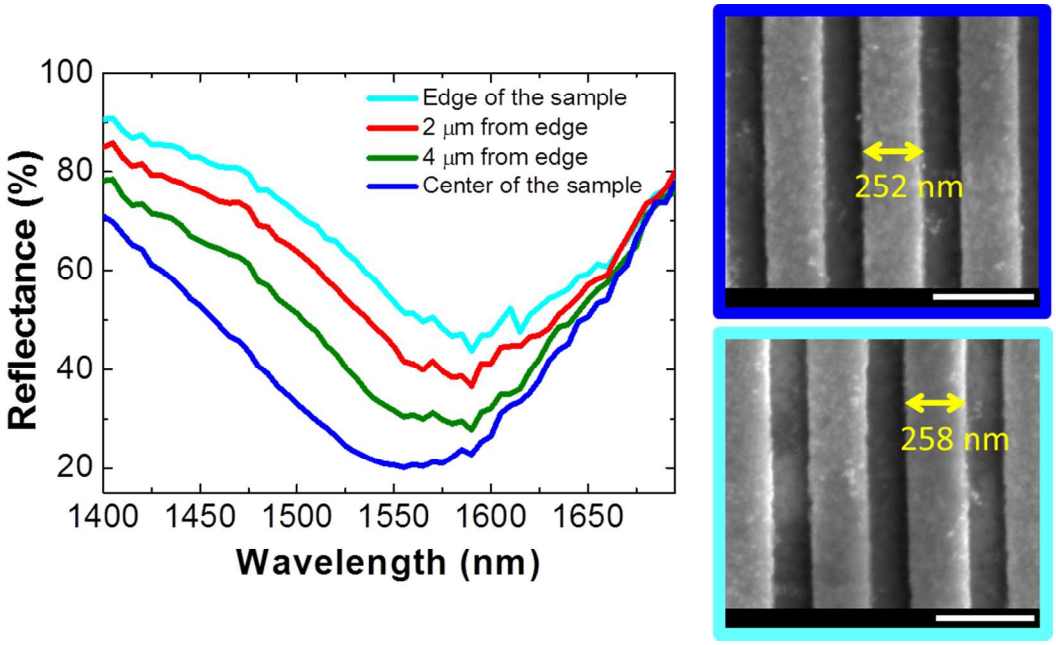

Figure S11. Measured reflectance spectra correspond to different positions of the metasurface. The SEM images show that the width of the stripes in the center of the sample is 252 nm while at the sample edge the stripe width is 258 nm.

In simulation, we keep all the parameters of materials and geometry the same except for the width of stripe antenna. The width is changed from 250 nm (center of the sample) to 257.5 nm in simulation for the edge of the sample. Figures S12a and S12b shows the reflectance and phase shift spectra as a function of applied bias in this case. The dashed line marks the position of a reflectance dip at 1580 at no applied bias (0V), showing a god match to the experimental reflectance spectra displayed in Fig. S11 (edge of the sample, cyan line). The phase shift under applied bias at 1573 nm shown in Fig. 3c (simulation, red dashed line) is obtained from the Fig. S12b (cross-section of wavelength of 1573 nm). Our calculations show good agreement with the experimental phase shift (Fig 3c).

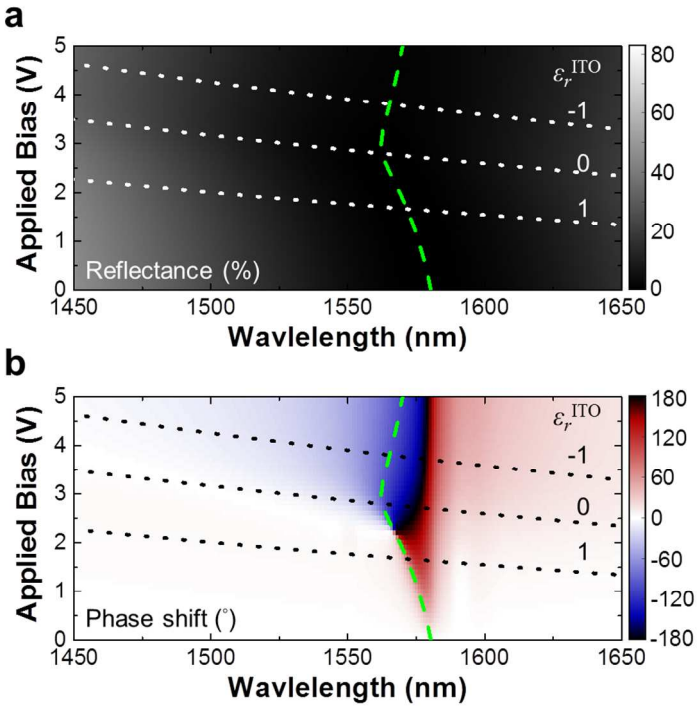

Figure S12. Simulated (a) reflectance and (b) phase shift due to gating as a function of wavelength and applied voltage. The dotted lines show points in V-λ parameter space for which permittivity of ITO equals from -1, 0 or 1 at the Al_2O_3/ITO interface, representing the ENZ region in the accumulation layer. The green dashed line marks the position of a reflectance dip corresponding to the magnetic dipole resonance. Note that the width of stripe antenna *w* is chosen as 257.5 nm corresponding to the wider stripe antennas at the edge of the sample.

8. Reflectance spectra of the metasurface under negative bias

Reflectance spectrum of the metasurface was also measured under a negative voltage bias between 0 V to -1.5 V as shown in Fig. S13. It is clear from the figure that the reflectance dip shifts to longer wavelengths when increasing absolute values of the applied negative voltage. This occurs due to further depletion of the ITO at the Al_2O_3/ITO interface as compared to the case when no voltage is applied. The shift of the resonance is less significant in this case as compared with the positive bias since applying negative bias results in increase of ε_r^{ITO} at

Al_2O_3/ITO interface, and shifts ENZ regions in the depletion layer further away from the magnetic dipole resonance.

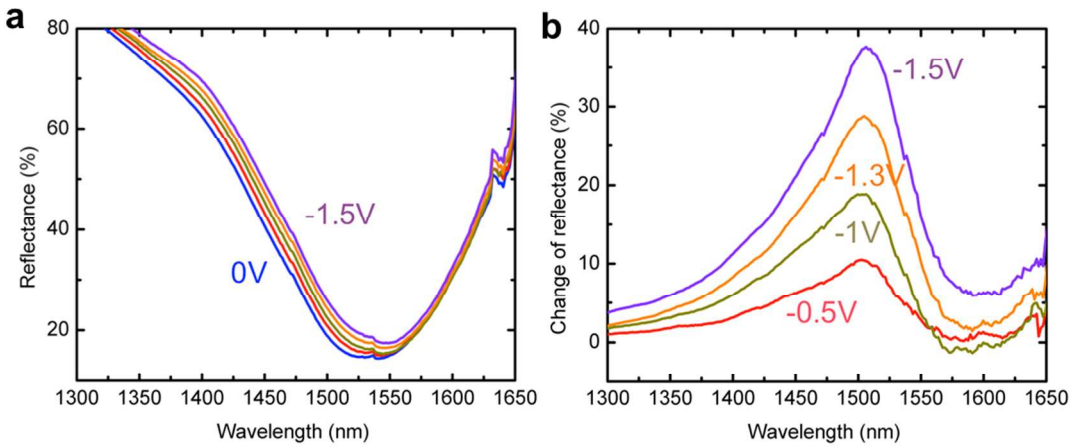

Figure S13. Measured reflectance spectrum (a) and relative reflectance change (b) from the metasurface for different negative biases.

9. High frequency AC modulation

The reflectance spectrum of the sample we used in the frequency modulation experiments is depicted in Fig. S14a (the width of the stripe antenna is w = 250 nm). As can be seen from the figure, the magnetic and electric resonances of the metasurface are located at ~ 1650 nm and ~ 1020 nm, respectively. By applying 2 V bias, the magnetic resonance shifts to shorter wavelengths, as expected from modeling, thus reducing the reflectance at the target wavelength of 1515 nm. Different biases are applied to the metasurface with a modulation speed of 2 MHz and the results are shown in Fig. S14b. It can be seen from the figure that up to ~ 15% amplitude modulation is obtained with an applied voltage of 2 V. The modulation speeds of the device with as high as 10 MHz were demonstrated (see Fig. 3d of the main text), clearly showing the ultrafast modulation based on the field-effect dynamics. The detection speed is currently limited by our detection method while we expect that modulation speeds up to >1 GHz may be achievable with appropriate high-frequency interconnect designs, due to the small device footprint and capacitance.[1,12]

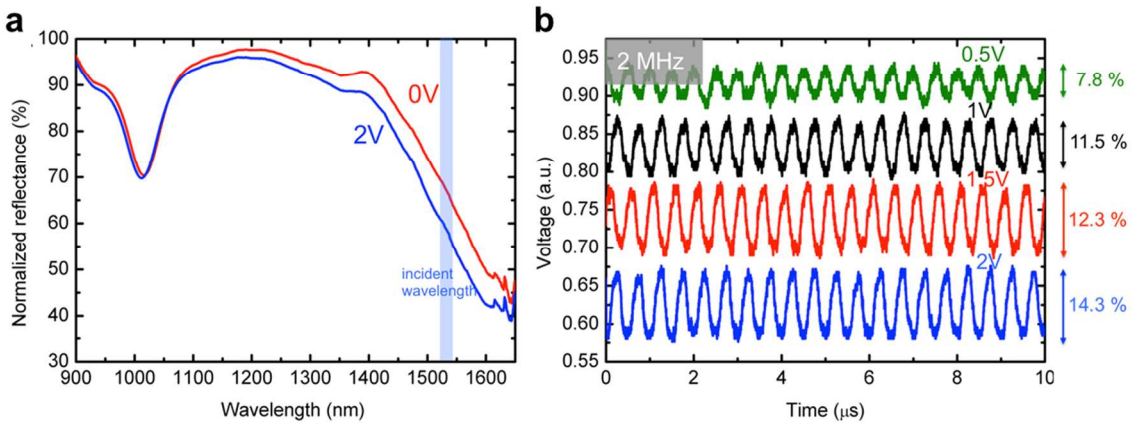

Figure S14. (a) Measured reflectance spectra of the sample for high frequency measurement at 0 V and 2 V bias. (b) Measured time response at 2 MHz modulations for different applied voltages.

10. IV characteristic of metasurface sample

A typical current-voltage response measurement for a field-effect tunable metasurface is given in Fig. S15. The voltage is applied between the gold back plane and the two top gold electrical pads. The current flowing between 5 nm of Al_2O_3 and 20 nm of ITO remains low (< 200 nA) under an applied bias of 2.5 V. The breakdown voltage for the devices varies from sample to sample taking values between 2.5 and 3 V, which correspond the breakdown electric fields of 5-6 MV/cm (with 5 nm insulating Al_2O_3 layer). These values are of the same order of magnitude as the values reported elsewhere.[13] Note that the breakdown voltage for the metasurface is lower than the planar structure without integrated nanostructures. We anticipate that the higher breakdown field of the metasurface device could be achieved by further treatment on the deposition and nano-patterning/lift off processes. It is worth mentioning that I-V curves do not demonstrate significant hysteretic behavior thus excluding the possibility of diffusion of gold into ITO or any ionic movement giving rise to this modulation.

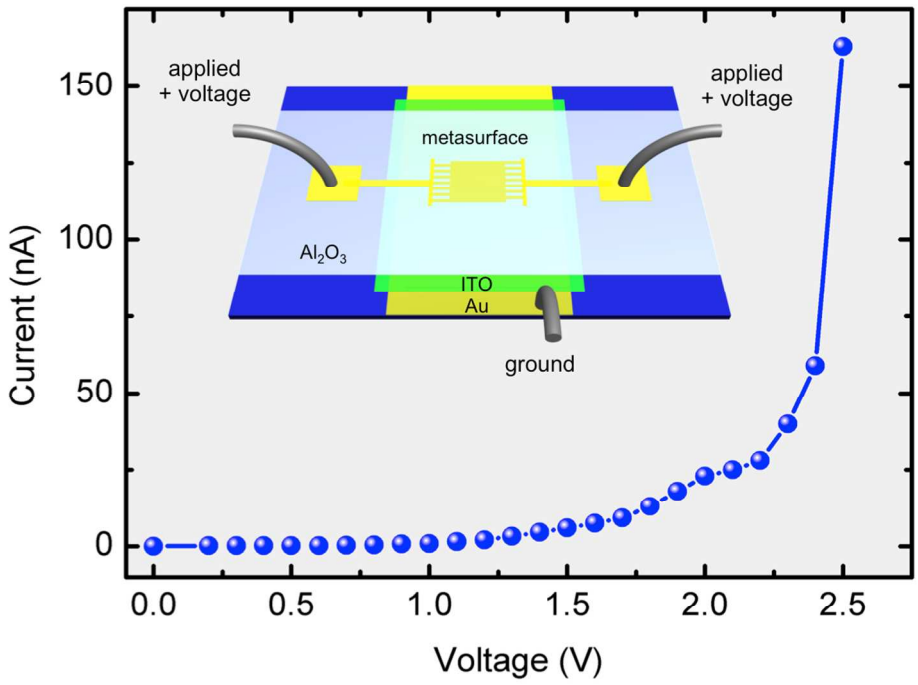

Figure S15. Measured IV response of the tunable metasurface. The voltage is applied between the gold backplane and two of the top gold electrodes.

As one can see from Fig. S15, the leakage current from the device is smaller than I = 175 nA at applied biases below 2.5 V. Using the fact that the measured metasurface operation period is $T = 10^{-7}$ s, we can estimate that the leakage sheet charge density $N_{sheet,L}$ (in units of electron charge per unit area) $N_{sheet,L} = \frac{I \times T}{e(\mathrm{S}/2)} \approx 3.5 \times 10^{10}\,\mathrm{cm}^{-2}$. Here e is the electron charge, S is the area of the whole device which is equal to 40 × 40 μm^2. When calculating sheet charge density, we normalize the accumulated charge to the half of the device area $S/2$ since only half of the device is covered by gold stripes. Further, by using values of the calculated device capacitance C = 14 fF/μm^2, we can estimate sheet charge density at Al_2O_3/ITO interface $N_{sheet,MOS}$ at applied bias of 2.5 V as $N_{sheet,MOS} = \frac{C \times V}{e} \approx 2.2 \times 10^{13}\,\mathrm{cm}^{-2}$. As one can see, $N_{sheet,L} << N_{sheet,MOS}$ hence the effect of the leakage current on our device performance is negligible.

References

1. Lee, H. W.; Papadakis, G.; Burgos, S. P.; Chander, K.; Kriesch, A.; Pala, R.; Peschel, U.; Atwater, H. A. *Nano Lett.* **2014**, 14, 6463-6468.

2. Melikyan, A.; Lindenmann, N.; Walheim, S.; Leufke, P. M.; Ulrich, S.; Ye, J.; Vincze, P.; Hahn, H.; Schimmel, T.; Koos, C.; et al. *Opt. Express* **2011**, 19, 8855-8869.

3. Michelotti, F.; Dominici, L.; Descrovi, E.; Danz, N.; Menchini, F. *Opt. Lett.* **2009**, 34, 839-841.

4. Krasavin, A. V.; Zayats, A. V. *Phys. Rev. Lett.* **2012**, 109, 053901.

5. Feigenbaum, E.; Diest, K.; Atwater, H. A. *Nano Lett.* **2010**, 10, 2111-2116.

6. Kim, J. S.; Cacialli, F.; Cola, A.; Gigli, G.; Gingolani, R. *Synthetic Met* **2000**, 111, 363-367.

7. Liu, X. G.; Park, J.; Kang, J. H.; Yuan, H. T.; Cui, Y.; Hwang, H. Y.; Brongersma, M. L. *Appl. Phys. Lett.* **2014**, 105, 181117.

8. Bayer, T. J. M.; Wachau, A.; Fuchs, A.; Deuermeier, J.; Klein, A. *Chemistry of Materials* **2012**, 24, 4503-4510.

9. Klein, A.; Korber, C.; Wachau, A.; Sauberlich, F.; Gassenbauer, Y.; Harvey, S. P.; Proffit, D. E.; Mason, T. O. *Materials* **2010**, 3, 4892-4914.

10. Yi, F.; Shim, E.; Zhu, A. Y.; Zhu, H.; Reed, J. C.; Cubukcu, E. *Appl. Phys. Lett.* **2013**, 102, 221102.

11. Maas, R.; Parsons, J.; Engheta, N.; Polman, A. *Nature Photonics* **2013**, 7, 907-912.

12. Sorger, V.; Lanzillotti-Kimura, N.; Ma, R.; Zhang, X. *Nanophotonics* **2012**, 1, 17.

13. Lin, H. C.; Ye, P. D.; Wilk, G. D. *Appl. Phys. Lett.* **2005**, 87, 182904.